Hyperspectral and LiDAR Fusion Using Extinction Profiles and Total Variation Component Analysis

Rasti, B.; Ghamis, I. P.; Gloaguen, R.;

Originally published:

April 2017

IEEE Transactions on Geoscience and Remote Sensing 99(2017), 3997-4007

DOI: https://doi.org/10.1109/TGRS.2017.2686450

Perma-Link to Publication Repository of HZDR:

https://www.hzdr.de/publications/Publ-25509

Hyperspectral and LiDAR Fusion Using Extinction Profiles and Total Variation Component Analysis

Behnood Rasti, *Member, IEEE*, Pedram Ghamisi, *Member, IEEE*, and Richard Gloaguen, *Member, IEEE*

***Abstract*— The classification accuracy of remote sensing data can be increased by integrating ancillary data provided by multisource acquisition of the same scene. We propose to merge the spectral and spatial content of hyperspectral images (HSIs) with elevation information from light detection and ranging (LiDAR) measurements. In this paper, we propose to fuse the data sets using orthogonal total variation component analysis (OTVCA). Extinction profiles are used to automatically extract spatial and elevation information from HSI and rasterized LiDAR features. The extracted spatial and elevation information is then fused with spectral information using the OTVCA-based feature fusion method to produce the final classification map. The extracted features have high dimension, and therefore OTVCA estimates the fused features in a lower dimensional space. OTVCA also promotes piece-wise smoothness while maintaining the spatial structures. Both attributes are important to provide homogeneous regions in the final classification maps. We benchmark the proposed approach (OTVCA-fusion) with an urban data set captured over an urban area in Houston/USA and a rural region acquired in Trento/Italy. In the experiments, OTVCA-fusion is evaluated using random forest and support vector machine classifiers. Our experiments demonstrate the ability of OTVCA-fusion to produce accurate classification maps while using fewer features compared with other approaches investigated in this paper.**

***Index Terms*— Extinction profiles (EPs), feature fusion, orthogonal total variation component analysis (OTVCA), random forest (RF), support vector machines (SVMs).**

I. Introduction

DUE to a recent increase in the availability of varied and complementary types of data from the immediate surface of the earth, it is now routinely possible to acquire and jointly utilize multisource data to improve the classification accuracy of land-cover classes. Such data captured either by active or passive remote sensors vary from spectral information [e.g., multispectral and hyperspectral images (HSIs)], to geometric information acquired by light detection and ranging (LiDAR) sensors. This availability makes it possible to integrate rich multisensor information to further improve object detection ability and classification performance.

The fusion of HSI and LiDAR was demonstrated to be beneficial for a huge number of applications such as shadow, height, and gap-related masking techniques [1]–[3], above-ground biomass estimation [4], microclimate modeling [5], quantifying riparian habitat structure [6], and fuel-type mapping [7]. In [8], the exploitation of multimodal data for earth observation has been reviewed. In addition, the joint use of LiDAR and HSI has shown promising results in terms of providing higher classification accuracy than the use of each source individually. To this end, in [9]–[14], spatial, contextual, and structural information obtained by LiDAR has been investigated along with spectral information captured by multispectral and hyperspectral sensors. Results significantly improved in terms of discrimination ability in forested and urban areas.

However, the automatic fusion of multiple types of data is not straightforward [12]. Moreover, the simple stacking of extracted features obtained by different sensors might cause the so-called *curse of dimensionality*, while the number of training samples is limited [15]–[20]. In order to solve this problem, several feature reduction techniques can be used [16]. This encourages one to develop an effective and efficient fusion approach to perform both dimensionality reduction and feature fusion at the same time [14].

Remote sensing images contain rich spatial information, which can be found useful for the classification task [16]. Recently, extinction profiles (EPs) [21] have been developed as an effective tool to extract spatial information from remote sensing images. It is worth mentioning that the threshold values for EPs can be set automatically, and they are also independent from the kind of the attribute being used (e.g., area, volume, etc.).

Total variation (TV) [22] is an efficient regularization technique for image processing, which has been widely used in remote sensing applications such as pansharpening [23], synthetic aperture radar denoising [24], HSI denoising [25], HSI compression [26], hyperspectral unmixing [27], [28], and HSI feature extraction [29]. In [30], a nonconvex TV-based regularization technique was proposed for HSI feature extraction. Also, it has been shown that the TV penalty as a spatial regularizer captures spatial correlation and promotes piece-wise smoothness that is of interest in HSI classification.

In this paper, a feature fusion technique for HSI and LiDAR is proposed, which includes two main stages, spatial feature extraction and fusion. EPs are used to extract spatial and

Manuscript received January 30, 2017; revised March 10, 2017; accepted March 16, 2017. *(Corresponding authors: Behnood Rasti; Pedram Ghamisi.)*

B. Rasti is with the Keilir Institute of Technology, 235 Reykjanesbær, Iceland, and also with the Department of Electrical and Computer Engineering, University of Iceland, 107 Reykjavik, Iceland (e-mail: behnood@keilir.net; behnood@hi.is).

P. Ghamisi is with the German Aerospace Center, Remote Sensing Technology Institute, Technische Universität München, Signal Processing in Earth Observation, 80333 Munich, Germany (e-mail: pedram.ghamisi@dlr.de).

R. Gloaguen is with Helmholtz-Zentrum Dresden-Rossendorf, Helmholtz Institute Freiberg for Resource Technology, 09599 Freiberg, Germany.

Color versions of one or more of the figures in this paper are available online at http://ieeexplore.ieee.org.

Digital Object Identifier 10.1109/TGRS.2017.2686450

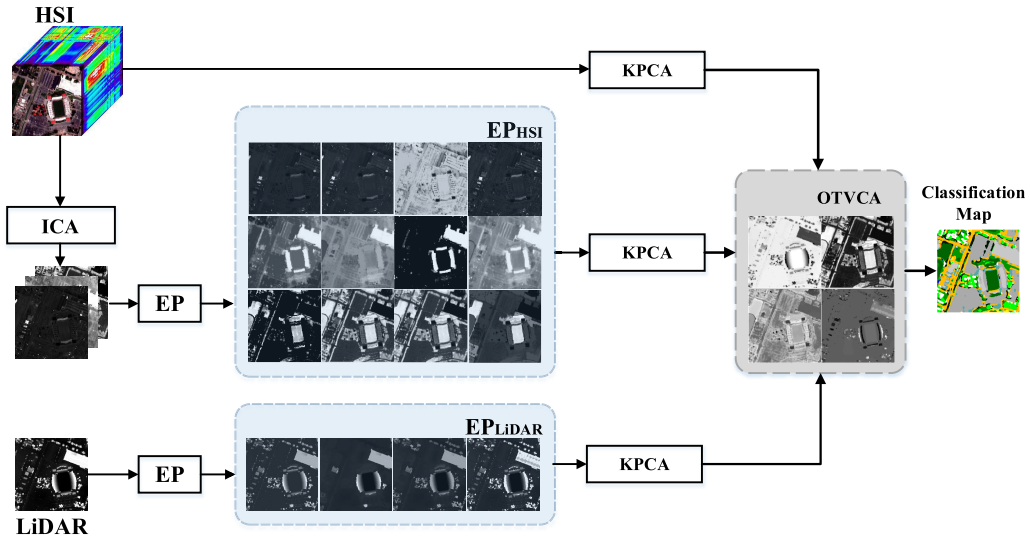

Fig. 1. Work flow of the proposed fusion method.

elevation information from HSI and LiDAR, respectively. Then, the extracted features from HSI and LiDAR are fused by utilizing the orthogonal TV component analysis (OTVCA) [30]. OTVCA estimates the fused features in a lower dimensional space while promotes piece-wise smoothness and maintains the spatial structures. The proposed fusion technique is evaluated based on classification accuracies obtained by applying both random forest (RF) and support vector machine (SVM) classifiers on the fused features. Both SVM and RF have been widely used for the classification of HSI since they can handle high dimensionality with a limited number of training samples, which is the common issue in remote sensing [16].

The rest of this paper is organized as follows. Section II describes the proposed OTVCA-fusion technique. The experiments are described in Section III. Section IV concludes this paper.

II. Methodology

In this section, after defining the notations used in this paper (Section II-A), the proposed fusion technique will be described in detail, which is composed of two parts, feature extraction using EPs (Section II-A) and feature fusion using OTCVA (Section II-C). Fig. 1 demonstrates the work flow of the proposed method.

A. Notation

In this paper, the numbers of bands and pixels in each band are denoted by p and n, respectively. Matrices are denoted by bold and capital letters, column vectors by bold letters, and the element placed in the ith row and jth column of matrix $\mathbf{X}$ by x_{ij} and the ith column by $\mathbf{x}_{(i)}$. Identity matrix of size $p \times p$ is denoted by $\mathbf{I}_p$. $\hat{\mathbf{X}}$ stands for the estimate of the variable $\mathbf{X}$, and $\mathbf{X}^m$ denotes the estimate of the variable $\mathbf{X}$ at the mth iteration.

B. Extinction Profiles (EPs)

Ghamisi *et al.* [21] proposed EPs by considering a set of connected filters, extinction filters, which can maintain relevant image extrema. Relevance here are defined based on the concept of the extinction value, proposed in [31]. Let $Max(\mathbf{X}) = \{M_1, M_2, \ldots, M_N\}$ represent the regional maxima of the gray scale image $\mathbf{X}$. Corresponding to each M_i, we can estimate an extinction value ϵ_i with respect to the increasing attribute being analyzed. For the input gray scale image $\mathbf{X}$, the extinction filter preserves the n maxima with the highest extinction values, $\mathrm{EF}^n(\mathbf{X}) = R_g^\delta(\mathbf{X})$, where $R_g^\delta(\mathbf{X})$ denotes the reconstruction by dilation [32] of the mask image. This is obtained by $g = \max_{i=1}^{n}\{M_i'\}$, in which max is the pixel-wise maximum operation. M_1' is the maximum with the highest extinction value, followed by M_2' with the second highest extinction value, and so on. For detailed description, please see [21].

EPs are achieved by applying several extinction filters, i.e., a sequence of thinning and thickening transformations, with progressively higher threshold values to extract spatial and contextual information of the input data. Thinning and thickening can be achieved from a max- and a min-tree, respectively [21]. The EP for the input gray scale image, $\mathbf{X}$, is obtained by

$$\mathrm{EP}(\mathbf{X}) = \left\{ \underbrace{\phi^{P_{\lambda_L}}(\mathbf{X}),\ \phi^{P_{\lambda_{L-1}}}(\mathbf{X}), \ldots, \phi^{P_{\lambda_1}}(\mathbf{X})}_{\text{thickening profile}}, \mathbf{X}, \underbrace{\gamma^{P_{\lambda_1}}(\mathbf{X}), \ldots, \gamma^{P_{\lambda_{L-1}}}(\mathbf{X}), \gamma^{P_{\lambda_L}}(\mathbf{X})}_{\text{thinning profile}} \right\} \quad (1)$$

where $P_\lambda : \{P_{\lambda_i}\}$ $(i = 1, \ldots, L)$ is a set of L ordered predicates (i.e., $P_{\lambda_i} \subseteq P_{\lambda_k}$, $i \leq k$). Please note that the number of extrema is considered as the predicates. ϕ and γ are thickening and thinning transformations, respectively.

In order to generalize and perform the EP to HSI, one can extract a few informative features from the whole dimensionality using an approach such as independent component analysis (ICA). Then the extracted features are considered as base images to produce EPs [33], entitled as extended EP (EEP).

In more detail, this approach reduces the dimensionality of the data from $E \subseteq \mathbf{Z}^n$ to $E' \subseteq \mathbf{Z}^m$ $(m \leq n)$ with a generic transformation $\Psi : E \rightarrow E'$ (i.e., ICA). Then, the EP can be performed on the most informative features $\mathbf{Q}_i$ $(i = 1, \ldots, m)$ of the extracted features, which can mathematically be given as

$$\text{EEP}(\mathbf{Q}) = \{\text{EP}(\mathbf{Q}_1), \text{EP}(\mathbf{Q}_2), \ldots, \text{EP}(\mathbf{Q}_m)\}. \quad (2)$$

The main reason for the use of ICA is that there is a high redundancy between hyperspectral bands. In this context, if any filtering approaches (e.g., morphological profiles (MPs) [34] or EPs [33]) are applied on all single bands, the number of redundant features will extremely be increased. Consequently, the effect of the Hughes phenomenon or the curse of dimensionality will be magnified, which downgrades classification results.

Extended multi-EP (EMEP) concatenates different EEPs (e.g., area, height, volume, diagonal of bounding box, and standard deviation on different extracted features) into a single stacked vector, which can be given as follows:

$$\text{EMEP} = \{\text{EEP}_{a_1}, \text{EEP}_{a_2}, \ldots, \text{EEP}_{a_w}\} \quad (3)$$

where $a_k, k = \{1, \ldots, w\}$, denotes different types of attributes. Due to the fact that different extinction attributes provide complementary spatial and contextual information, the EMEP has a greater ability in extracting spatial information than a single EP. For more detail, please see [21], [33]. It is important to note that the EMEP and EP require almost the same computational time since the most time demanding part is on the construction of the max-tree and min-tree, which are computed only once for each gray scale image [21], [33].

EPs work naturally with the number of extrema. EPs provide better results in terms of classification accuracies than the ones obtained by attribute profiles. Moreover, they address the issue of adjusting threshold values, which was the main shortcoming of the conventional APs [21].

C. Feature Fusion Using Orthogonal Total Variation Component Analysis

Let **HSI** be the input hyperspectral data set, which provides detailed spectral information. $\mathbf{EP}_{\text{HSI}}$ represents the spatial features produced by EPs on the first three independent components. $\mathbf{EP}_{\text{LiDAR}}$ is the elevation information obtained by EPs on the LiDAR derived digital surface model (DSM). To fuse the aforementioned features, one needs to normalize the number of dimensionalities to put the same weight on each type of the features and reduce the computational cost and noise throughout the feature space [35]. To do so, kernel PCA [36] was used as an effective tool to reduce the dimensionality of each type of features independently, since it can represent a higher order complex and nonlinear distribution in a fewer number of dimensions to address Hughes phenomenon [15] and high computational cost. The normalized dimension of **HSI**, $\mathbf{EP}_{\text{HSI}}$, and $\mathbf{EP}_{\text{LiDAR}}$ is automatically set to the smallest dimension of the above-mentioned features. For example, for the Houston data, this value is set to 71 [9]. We show the normalized features extracted from LiDAR and HSI with matrices $\mathbf{F}_{\text{HSI}}$ and $\mathbf{F}_{\text{LiDAR}}$, respectively, and the HSI with matrix $\mathbf{H}$.

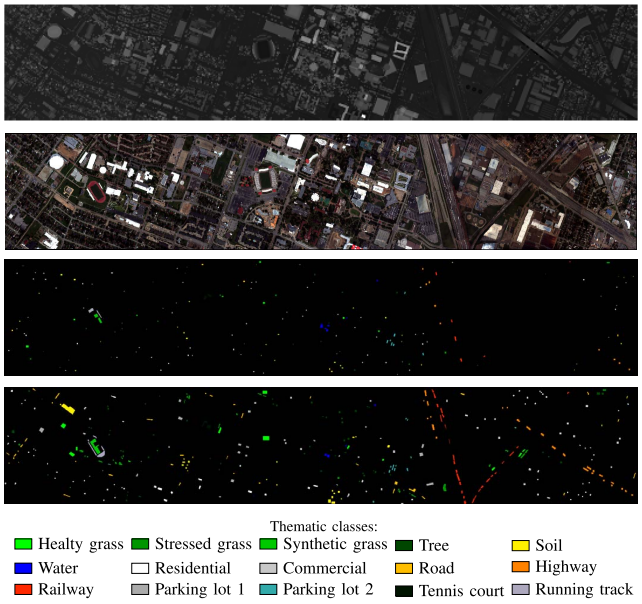

Fig. 2. Houston. (Top to bottom) LiDAR-derived rasterized data set; a color composite representation of the HSI using bands 64, 43, and 22 as R, G, and B, respectively; training samples; test samples; and legend of different classes.

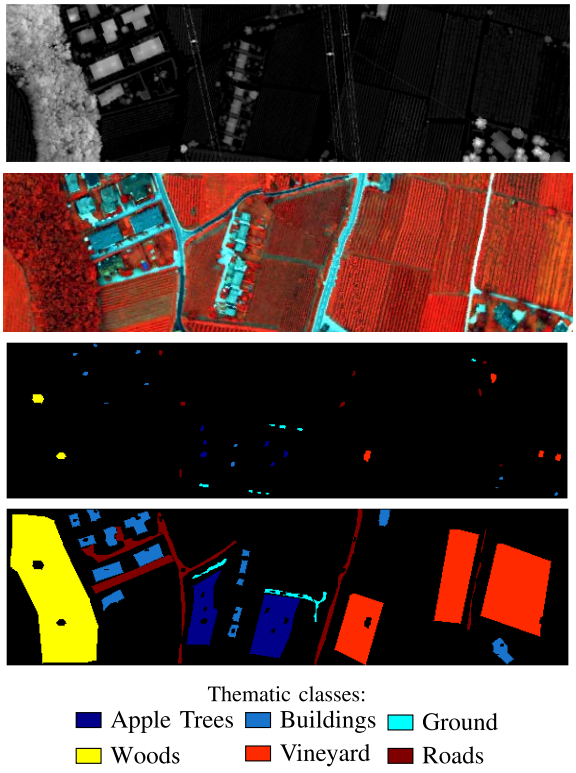

Fig. 3. Trento. (Top to bottom) LiDAR-derived rasterized data set; a color composite representation of the HSI using bands 40, 20, and 10, as R, G, and B, respectively; training samples; test samples; and legend of different classes.

Extracted features from HSI and LiDAR are highly redundant. In order to reduce the features' redundancy, we propose

TABLE I

HOUSTON: CLASSIFICATION ACCURACIES OBTAINED BY DIFFERENT APPROACHES USING RF AND SVM. THE METRICS AA AND OA ARE REPORTED IN PERCENTAGE. KAPPA COEFFICIENT IS OF NO UNITS. THE BEST RESULT IS SHOWN IN BOLD

		LiDAR (1)		**HSI** (144)		$\mathbf{EP}_{\text{LiDAR}}(71)$		$\mathbf{EP}_{\text{HSI}}(213)$		$\mathbf{EP}_{\text{LiDAR+HSI}}(284)$		OTVCA-fusion (50)	
Class name	Train./Test	SVM	RF	SVM	RF	SVM	RF	SVM	RF	SVM	RF	SVM	RF
Grass Healthy	198/1053	11.68	13.49	**83.48**	83.38	57.36	74.26	79.39	77.49	79.39	78.06	79.77	80.63
Grass Stressed	190/1064	0.00	16.26	96.43	98.40	40.79	61.75	78.85	78.48	80.36	84.96	97.84	**99.62**
Grass Synthetic	192/505	87.13	56.63	99.80	98.02	98.61	97.23	**100.00**	**100.00**	**100.00**	**100.00**	**100.00**	**100.00**
Tree	188/1056	51.80	44.03	**98.77**	97.54	92.33	58.14	87.78	82.77	95.83	95.45	96.02	96.02
Soil	186/1056	12.12	58.05	98.11	96.40	83.43	82.10	**99.81**	97.73	**99.81**	98.77	98.67	99.43
Water	182/143	78.32	58.04	95.10	**97.20**	78.32	83.22	95.80	95.80	95.80	95.80	95.80	95.80
Residential	196/1072	56.90	39.09	**89.09**	82.09	55.22	77.33	85.17	73.23	80.41	73.41	88.90	86.01
Commercial	191/1053	13.11	29.53	45.87	40.65	29.06	68.28	65.15	59.92	90.41	85.28	87.65	**93.54**
Road	193/1059	14.92	13.60	82.53	69.78	67.33	59.40	89.90	83.00	89.80	93.96	87.35	**97.07**
Highway	191/1036	8.30	11.29	**83.20**	57.63	61.39	66.89	51.54	64.09	56.66	67.08	60.33	68.53
Railway	181/1054	72.68	40.42	83.87	76.09	99.72	**99.91**	87.76	84.72	90.70	90.89	99.34	98.86
Parking Lot 1	192/1041	0.00	9.99	70.99	49.38	63.11	64.75	84.34	78.10	89.91	88.57	97.69	**100.00**
Parking Lot 2	184/285	12.28	15.09	70.53	61.40	49.12	58.60	**84.56**	77.89	**84.56**	76.14	80.35	74.74
Tennis Court	181/247	97.57	80.16	**100.00**	99.60	**100.00**	**100.00**	**100.00**	99.60	**100.00**	**100.00**	**100.00**	**100.00**
Running Track	187/473	27.91	75.90	97.46	97.67	74.21	87.74	97.25	99.37	98.10	99.79	**100.00**	**100.00**
OA		28.82	31.83	84.69	77.47	67.2	73.42	85.82	80.36	86.87	86.98	90.33	**92.45**
AA		36.31	37.43	86.34	80.34	70.00	75.97	83.08	83.47	88.78	88.54	91.31	**92.68**
κ		0.2422	0.2677	0.8340	0.7563	0.6440	0.7120	0.8168	0.7876	0.8577	0.8592	0.8950	**0.9181**

TABLE II

TRENTO: CLASSIFICATION ACCURACIES OBTAINED BY DIFFERENT APPROACHES USING RF AND SVM. THE METRICS AA AND OA ARE REPORTED IN PERCENTAGE. KAPPA COEFFICIENT IS OF NO UNITS. THE BEST RESULT IS SHOWN IN BOLD

		LiDAR (1)		**HSI** (63)		$\mathbf{EP}_{\text{LiDAR}}(71)$		$\mathbf{EP}_{\text{HSI}}(213)$		$\mathbf{EP}_{\text{LiDAR+HSI}}(284)$		OTVCA-fusion (50)	
Class name	Train./Test	SVM	RF	SVM	RF	SVM	RF	SVM	RF	SVM	RF	SVM	RF
Apple trees	129/3905	37.10	42.50	88.40	86.20	98.56	96.06	99.93	97.82	99.95	97.62	**100.00**	99.95
Buildings	125/2778	41.40	51.30	82.60	85.90	96.21	98.42	97.97	94.25	97.24	96.80	98.45	**98.81**
Ground	105/374	0.00	34.20	97.60	96.80	70.15	72.03	97.08	94.99	96.45	94.36	96.26	**99.47**
Wood	154/8969	67.40	52.60	96.90	95.70	98.64	99.45	99.81	99.22	99.57	99.97	**100.00**	**100.00**
Vineyard	184/10317	87.60	46.50	77.10	80.10	58.39	69.89	99.57	98.76	99.26	99.10	98.55	**99.99**
Roads	122/3252	79.90	32.40	67.90	65.00	73.06	70.79	69.03	76.15	94.27	94.55	96.07	**96.26**
OA		63.30	46.70	84.55	84.92	67.20	85.17	96.28	95.90	98.68	98.39	98.89	**99.48**
AA		46.14	43.31	85.14	85.01	70.00	84.43	93.89	93.53	97.79	97.06	98.22	**99.08**
κ		0.5039	0.335	0.7965	0.8004	0.6440	0.8099	0.9505	94.53	0.9824	0.9785	0.9851	**0.9931**

a low-rank model for the fused features. In other words, the extracted features from LiDAR and HSI can be represented in a space of lower dimension. Note that this redundancy of features can affect the classification results due to the Hughes phenomenon and also fused features are expected to have a lower dimension.

As a result, a low-rank model is suggested as

$$\mathbf{F} = \mathbf{A}\mathbf{V}^T + \mathbf{N} \tag{4}$$

where $\mathbf{F} = [\mathbf{f}_{(i)}]$ is an $n \times p$ matrix containing the vectorized features at band i in its ith column, $\mathbf{V}$ is an unknown subspace (low-rank) basis ($p \times r$), $\mathbf{A} = [\mathbf{a}_{(i)}]$ contains the ith vectorized unknown fused feature in its ith column, and $\mathbf{N} = [\mathbf{n}_{(i)}]$ is an $n \times p$ matrix containing the vectorized noise and error at band i in its ith column. Note that r is the number of fused features ($1 \leq r \leq p$), and $\mathbf{F} = [\mathbf{F}_{\text{HSI}}, \mathbf{H}, \mathbf{F}_{\text{LiDAR}}]$ contains hyperspectral bands and features extracted from both HSI and LiDAR rasterized data.

In (4), it is assumed that the fused features, $\mathbf{F}$, and the basis matrix, $\mathbf{V}$, are unknown, and therefore they both need to be estimated. To preserve the spatial structure of the features and promote piece-wise smoothness on the fused features, we use OTVCA [30], which is based on solving the following TV penalized least squares problem:

$$\begin{aligned}(\hat{\mathbf{A}}, \hat{\mathbf{V}}) = \arg\min_{\mathbf{A},\mathbf{V}} \; J(\mathbf{A}, \mathbf{V}) = \arg\min_{\mathbf{A},\mathbf{V}} \; & \frac{1}{2}\|\mathbf{F} - \mathbf{A}\mathbf{V}^T\|_F^2 \\ & + \lambda \sum_{i=1}^{r} \left\| \sqrt{(\mathbf{D}_h \mathbf{a}_{(i)})^2 + (\mathbf{D}_v \mathbf{a}_{(i)})^2} \right\|_1 \quad \text{s.t. } \mathbf{V}^T\mathbf{V} = \mathbf{I}_r\end{aligned} \tag{5}$$

where $\mathbf{D}_h$ and $\mathbf{D}_v$ are the matrix operators for calculating the first-order vertical and horizontal differences, respectively, for a vectorized image. For an image of size $n_1 \times n_2$, we have $\mathbf{D}_h = \mathbf{R} \otimes \mathbf{I}_{n_1}$ and $\mathbf{D}_v = \mathbf{I}_{n_2} \otimes \mathbf{R}$, where $\mathbf{R}$ is the first-order difference matrix.

D. Estimation

A cyclic descent (CD) algorithm given in [30] is used to solve (5) called OTVCA-CD, which solves the nonconvex problem (5) with respect to one matrix at a time while the other matrix is assumed to be fixed. Therefore, OTVCA-CD consists of the following two steps.

TABLE III

ASSESSMENT OF THE SIGNIFICANCE OF THE CLASSIFICATION ACCURACIES (z_{rc}, WHERE r AND c INDICATE ROW AND COLUMN, RESPECTIVELY) OBTAINED BY APPLYING RF AND SVM ON THE UNIVERSITY OF HOUSTON DATA SET USING DIFFERENT METHODS

	RF				SVM			
	HSI	**EP**$_{\text{LiDAR}}$	**EP**$_{\text{HSI}}$	**EP**$_{\text{LiDAR+HSI}}$	**HSI**	**EP**$_{\text{LiDAR}}$	**EP**$_{\text{HSI}}$	**EP**$_{\text{LiDAR+HSI}}$
EP$_{\text{LiDAR}}$	-7.27				-38.00			
EP$_{\text{HSI}}$	2.23	10.48			-16.35	24.94		
EP$_{\text{LiDAR+HSI}}$	15.89	24.03	21.77		-0.79	38.70	20.87	
OTVCA-fusion	36.36	44.94	40.17	30.01	15.81	50.09	32.61	20.08

TABLE IV

ASSESSMENT OF THE SIGNIFICANCE OF THE CLASSIFICATION ACCURACIES (z_{rc}, WHERE r AND c INDICATE ROW AND COLUMN, RESPECTIVELY) OBTAINED BY APPLYING RF AND SVM ON THE TRENTO DATA SET USING DIFFERENT METHODS

	RF				SVM			
	HSI	**EP**$_{\text{LiDAR}}$	**EP**$_{\text{HSI}}$	**EP**$_{\text{LiDAR+HSI}}$	**HSI**	**EP**$_{\text{LiDAR}}$	**EP**$_{\text{HSI}}$	**EP**$_{\text{LiDAR+HSI}}$
EP$_{\text{LiDAR}}$	1.08				-11.58			
EP$_{\text{HSI}}$	54.31	49.36			58.46	62.89		
EP$_{\text{LiDAR+HSI}}$	59.98	58.18	17.44		63.34	71.45	16.78	
OTVCA-fusion	65.68	65.30	28.31	20.11	63.44	72.48	16.35	1.94

1) A-Step: When matrix $\mathbf{V}$ is fixed, it can be shown that the minimization problem (5) can be considered as r separable TV regularization problems, which can be solved using split Bregman iterations as

$$\mathbf{A}^{m+1} = \text{SplitBregman}(\mathbf{G}, \lambda) \tag{6}$$

where $\mathbf{G} = [\mathbf{g}_{(i)}] = \mathbf{F}\mathbf{V}^m$.

2) V-Step: When matrix $\mathbf{A}$ is fixed, it can be shown that the minimization problem (5) turns to an orthogonal (low-rank) Procrustes problem where the solution is given by a low-rank Procrustes rotation as

$$\mathbf{V}^{m+1} = \mathbf{P}\mathbf{Q}^T$$

where matrices $\mathbf{P}$ and $\mathbf{Q}$ are given by the following singular value decomposition (SVD):

$$\mathbf{F}^T\mathbf{A}^{m+1} = \mathbf{P}\Sigma\mathbf{Q}^T$$

where Σ is a diagonal matrix that contains the singular values of $\mathbf{F}^T\mathbf{A}^{m+1}$. The resulting algorithm is summarized in Algorithm 1. For more details, see [30].

Algorithm 1 OTVCA-CD

Input:
$\mathbf{F}$: Extracted Features,
r: Number of fused features,
λ: TV regularization tuning parameter,
ϵ: Tolerance values.
Output:
$\hat{\mathbf{A}}$: Fused features estimated,
$\hat{\mathbf{V}}$: Projection matrix estimated.
Initialization;$\mathbf{V}^0$,
while $\left\|\mathbf{A}^{m+1} - \mathbf{A}^m\right\|_F \leq \epsilon$ **do**
  A-step :
  $\mathbf{G} = \mathbf{F}\mathbf{V}^m$,
  $\mathbf{A}^{m+1} = \text{SplitBregman}(\mathbf{G}, \lambda)$,
  V-step :
  $\mathbf{F}^T\mathbf{A}^{m+1} = \mathbf{P}\Sigma\mathbf{Q}^T$,
  $\mathbf{V}^{m+1} = \mathbf{P}\mathbf{Q}^T$,
end

III. EXPERIMENTAL RESULTS

A. Data Description

1) Houston Data: The size of the HSI and DSM is 349 × 1905 with a spatial resolution of 2.5 m. The HSIs encompass 144 spectral bands ranging 0.38–1.05 μm. Fig. 2 demonstrates a color composite representation of the HSI and the corresponding training and test samples. Table I details the number of training and test samples of different classes.

2) Trento Data: The second data set is captured over a rural area in the south of the city of Trento, Italy. The size of the coregistered DSM and HSI is 600 by 166 pixels with a spatial resolution of 1m. The HSI consists of 63 bands ranging from 0.40 to 0.98 μm. Fig. 3 demonstrates a color composite representation of the HSI and the corresponding training and test samples. Table II gives information about the number of training and test samples for different classes of interest.

B. Algorithm Setup

For the EPs, one needs to define only the number of desired levels (s) as the whole process is automatic. To do so, we have used exactly the same setup investigated in [33], which demonstrates that the EPs are data set distribution independent, and one can consider the same values for diverse data captured by different sensors. In this context, in order to generate the EP for area, volume, and diagonal of the bounding box, the values of n used to generate the profile are automatically given by $\lfloor 3^j \rfloor$, where $j = 0, 1, \ldots, s-1$. The size of the EPs is $2s+1$, since the original image should also be included in the profile. The profiles were computed

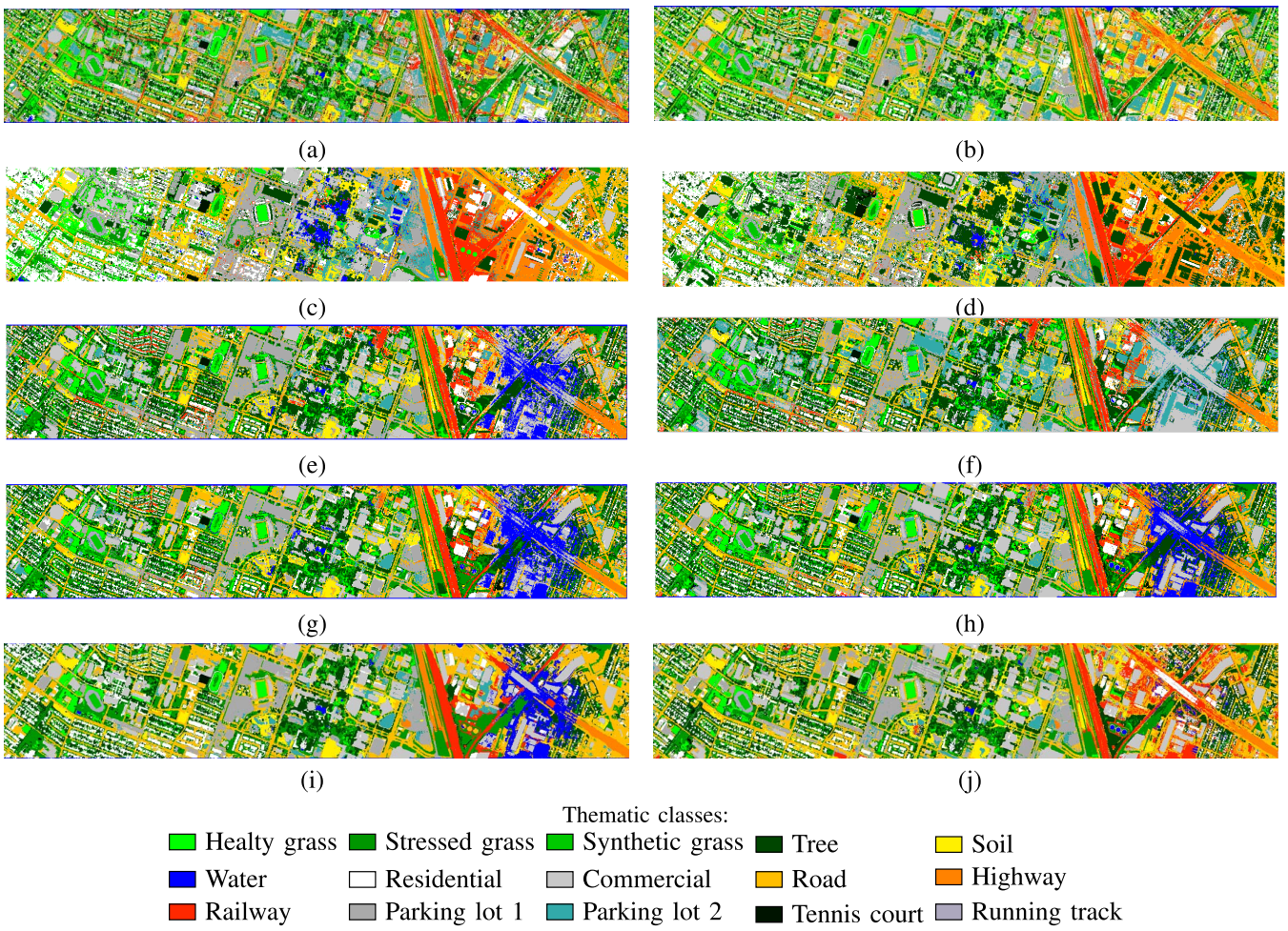

Fig. 4. Classification maps for the Houston data set. (a) Outputs of RF on **HSI**. (b) Output of SVM on **HSI**. (c) Output of RF on $\mathbf{EP}_{\text{LiDAR}}$. (d) Outputs of SVM on $\mathbf{EP}_{\text{LiDAR}}$. (e) Output of RF on $\mathbf{EP}_{\text{HSI}}$. (f) Outputs of SVM on $\mathbf{EP}_{\text{HSI}}$. (g) Output of RF on $\mathbf{EP}_{\text{LiDAR+HSI}}$. (h) Outputs of SVM on $\mathbf{EP}_{\text{LiDAR+HSI}}$. (i) Output of the proposed method using RF. (j) Output of the proposed method using SVM.

using the four-connected connectivity rule. Here, s is set to seven, as suggested in [33].

OTVCA is initialized as suggested in [30]. The tuning parameter λ indicates the level of smoothness. In the experiments, λ is set to one percent of the intensity range of the features extracted.

In terms of the SVM, a radial basis function (RBF) kernel is used. The optimal hyperplane parameters C (parameter that controls the amount of penalty during the SVM optimization) and γ (spread of the RBF kernel) have been traced in the range of $C = 10^{-2}, 10^{-1}, \ldots, 10^{4}$ and $\gamma = 2^{-3}, 2^{-2}, \ldots, 2^{4}$ using fivefold cross validation.

For the RF, the number of trees is set to 300. The number of the prediction variable is set approximately to the square root of the number of input bands.

In this paper, overall accuracy (OA), average accuracy (AA), kappa coefficient, and CPU processing time are used to compare the classification approaches from different aspects. In addition, in order to evaluate the significance of the classification accuracies obtained using different approaches, we use a statistical test. Since the samples were used for two different classifications are not independent, we evaluate the significance of two classification results with McNemar's test, which is given by [37]

$$z_{12} = \frac{f_{12} - f_{21}}{\sqrt{f_{12} + f_{21}}}$$

where f_{ij} is the number of correctly classified samples in classification i and incorrectly in classification j. McNemar's test is based on the standardized normal test statistic, and therefore the null hypothesis that is "no significant difference" is rejected at the widely used $p = 0.05$ ($|z| > 1.96$) level of significance.

For the sake of simplicity, the following names are used in the experimental part: LiDAR and HSI show the classification accuracies of the LiDAR-derived DSM and HSI, respectively. $\mathbf{EP}_{\text{LiDAR}}$ and $\mathbf{EP}_{\text{HSI}}$ show the classification accuracies of EPs applied to LiDAR and HSI. $\mathbf{EP}_{\text{LiDAR+HSI}}$ refers to the classification accuracies of EPs applied to the stack of LiDAR and HSI.

C. Classification Experiments

The classification results are given in Tables I and II for the Houston and Trento data sets, respectively. The results are

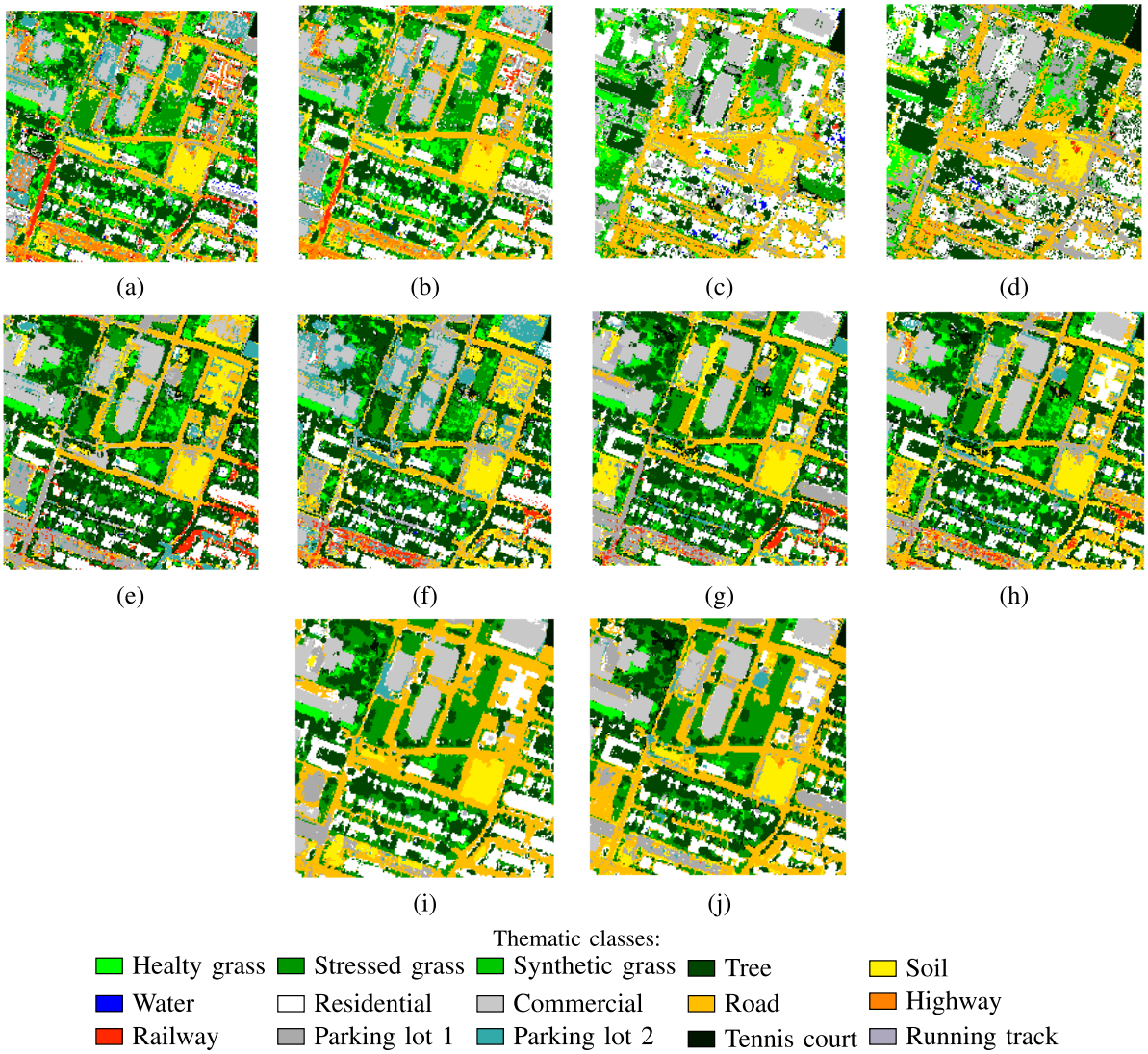

Fig. 5. Classification maps for the Houston data set. (a) Outputs of RF on **HSI**. (b) Output of SVM on **HSI**. (c) Output of RF on $\mathbf{EP}_{\text{LiDAR}}$. (d) Outputs of SVM on $\mathbf{EP}_{\text{LiDAR}}$. (e) Output of RF on $\mathbf{EP}_{\text{HSI}}$. (f) Outputs of SVM on $\mathbf{EP}_{\text{HSI}}$. (g) Output of RF on $\mathbf{EP}_{\text{LiDAR+HSI}}$. (h) Outputs of SVM on $\mathbf{EP}_{\text{LiDAR+HSI}}$. (i) Output of the proposed method using RF. (j) Output of the proposed method using SVM.

compared based on class accuracies, OA, AA, and kappa coefficient (κ). The SVM parameters selected by cross validation for Houston are $C = 100$ and for $\gamma = 0.5$ and Trento are $C = 1$ and $\gamma = 0.5$.

As can be seen from Table I, the consideration of the spatial information extracted by the EP can significantly improve classification accuracies compared with the situations where the SVM and RF have directly been applied to the input data sets. For instance, in the case of using SVM, applying EP on the LiDAR (71 features) improves the OA by almost 38%. In the case of the HSI, due to the rich spectral information, the consideration of the EPs slightly improves the OA by almost 1% and 3%, using SVM and RF, respectively. Due to the fact that the $\mathbf{EP}_{\text{HSI}}$ has been constructed only on three ICs, it does not fully consider rich spectral information provided by the whole dimensionality of the HSI. In this context, **HSI** can classify different types of grasses better than $\mathbf{EP}_{\text{HSI}}$. $\mathbf{EP}_{\text{LiDAR+HSI}}$ outperforms the individual use of each data in terms of OA, AA, and kappa, which confirms that HSI and LiDAR provide complement information to differentiate different classes of interest. The proposed approach provides the best classification accuracy among all the approaches considered in this paper. OTVCA-fusion method clearly captures the redundant information existing in the HSI and the profiles and leads to the accuracy of over 90%. A similar trend can be seen in the case of using RF, where the OA obtained from the 50 fused features using OTVCA reaches over 92%, which is 5% more than the integrated profiles having 284 features. In addition, since the proposed method considers all spectral, spatial, and contextual information, it reveals a promising performance in terms of class specific accuracy and provides the best classification results for classes Grass Stressed, Grass Synthetic, Commercial, Road, Parking Lot 1, Tennis Court, and Running Track.

As can be seen from Table II, in the case of the Trento data set, the use of the EP can significantly improve classification accuracies due to the fact that the EP can effectively

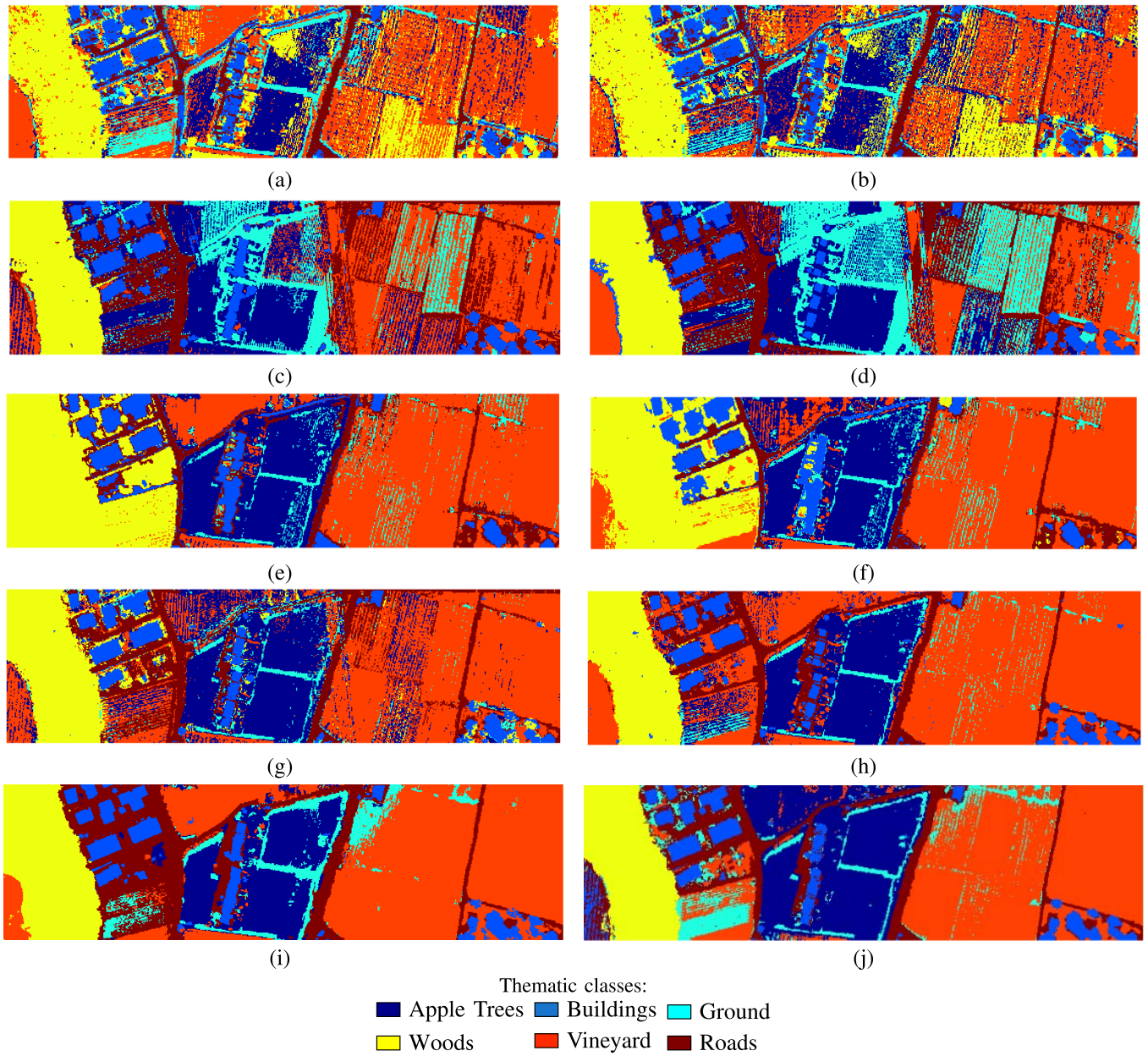

Fig. 6. Classification maps for the Trento data set. (a) Outputs of RF on **HSI**. (b) Output of SVM on **HSI**. (c) Output of RF on $\mathbf{EP}_{\text{LiDAR}}$. (d) Outputs of SVM on $\mathbf{EP}_{\text{LiDAR}}$. (e) Output of RF on $\mathbf{EP}_{\text{HSI}}$. (f) Outputs of SVM on $\mathbf{EP}_{\text{HSI}}$. (g) Output of RF on $\mathbf{EP}_{\text{LiDAR+HSI}}$. (h) Outputs of SVM on $\mathbf{EP}_{\text{LiDAR+HSI}}$. (i) Output of the proposed method using RF. (j) Output of the proposed method using SVM.

extract spatial and contextual information. In addition, for both RF and SVM classifiers, the 50 fused features obtained by applying OTVCA improve the classification accuracies compared with the integrated profiles (284 features). Moreover, the proposed method using RF provides the best class specific accuracy for almost all classes.

Overall, Tables I and II show that OTVCA-fusion improves the classification accuracies using fewer number of features for both rural and urban data sets. Moreover, from Tables I and II, it can be seen that the RF provides higher OA, AA, and kappa coefficients than SVM.

The assessment of the significance of the difference between the OAs based on McNemar's test is given in Tables III and IV for the University of Houston and Trento data sets, respectively. From Tables I and II, it is clear that the classification accuracies obtained from LiDAR are considerably low, and therefore they have not been included in the signification assessments. As can be seen in Tables III and IV, in the case of using RF, the improvements of OAs yielded by OTVCA-fusion are statistically significant for both data sets compared with the other methods. In the case of using SVM, the results confirm that the improvements of the OAs yielded by OTVCA-fusion for both data sets are also statistically significant compared with the other methods except for the Trento data set when it is compared with $\mathbf{EP}_{\text{LiDAR+HSI}}$.

The classification maps obtained by different approaches on the Houston data are shown in Fig. 4. From Fig. 4, it can be seen that the proposed fusion technique provides classi-

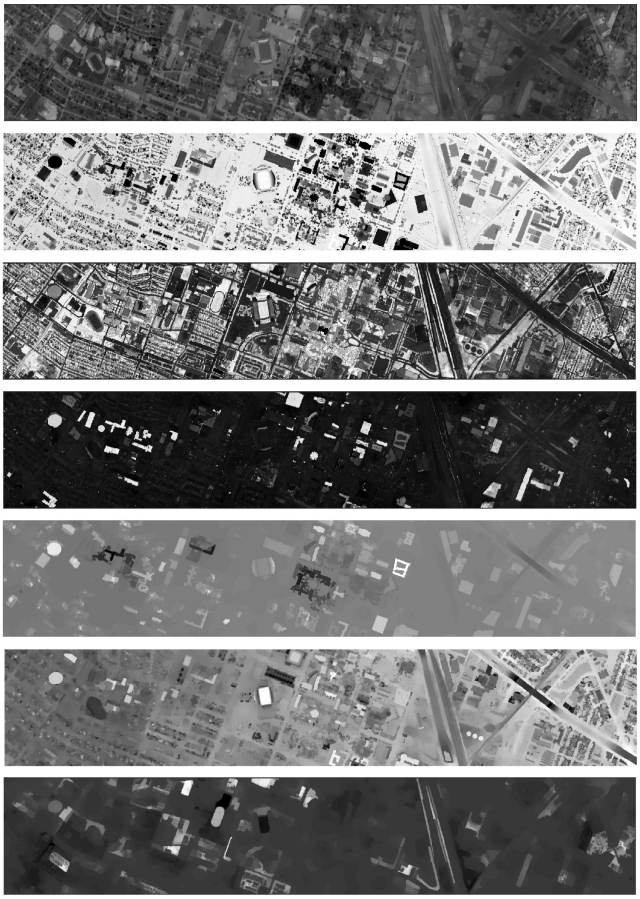

Fig. 7. HSI and LiDAR features of the Houston data set fused by OTVCA-fusion and used for the classification tasks. From top to bottom, the numbers of features are 1, 2, 3, 5, 15, 27, and 45.

fication maps having homogeneous regions while preserving the structures, which is greatly of the interest specifically in the case of urban data sets. This is because of using TV that promotes smoothness while preserves the structures existing in the features. In this paper, although the cloud shadow was removed from the original data to a great extent, when ICA is performed to the enhanced hyperspectral data to produce base features for EPs, the shadow effect is partially appeared on the second IC. This is the reason that the cloud shadow slightly downgrades the quality of the classification maps obtained by the proposed approach. In other words, pixels on the right sides that are classified as water most probably are missclassified. This is due to the attenuation of the spectra in the shadow area.

In order to have a more precise evaluation of the obtained classification maps, Fig. 5 is provided, which shows a close-up of the resulting classification maps obtained by studied approaches on the Houston data. As can be seen, the consideration of the EPs can homogenize the classification maps by extracting the structures of different objects and reducing the salt and pepper appearance of the labeled pixels compared with a situation where only spectral information is taken into account. This has been further improved by the proposed approach, which uses OTVCA to fuse spectral, spatial, and elevation information. In Fig. 5, it is evident that the proposed method can extract the shape of different objects more precisely than the other investigated approaches, while at the same time, it significantly reduces the noisy behavior of the labeled pixels compared with EPs and HSI. A few features obtained by the proposed fusion technique and used for the classification of the Houston data set are shown in Fig. 7.

Fig. 6 demonstrates the classification maps obtained by different approaches on the Trento data set. The same trend as the Houston data can also be found for the Trento data, where the proposed approach provides a more precise classification map than the ones obtained by other approaches. Regarding the left side of Trento, visual comparison confirms that SVM applied on OTVCA-fusion has missclassified a region and labeled as buildings (also note that the improvement of the classification accuracies obtained by the test samples is not significant in this case). Also, the visual comparison of RF applied on OTVCA-fusion show a considerable improvement, which confirms the accuracies obtained by the test samples and the results from McNemar's test.

Comparing the results given for the Houston University and Trento data sets shows that the improvement of the classification accuracies in the case of Trento that is rural data set is more significant than the Houseton University data set. This could be due to the lower spatial resolution in rural area where the TV component analysis should be very effective to promote piecewise smooth regions.

Table V compares the CPU processing time (in seconds) consumed by different techniques applied on Trento. As can be seen, OTVCA-fusion is computationally expensive compared with the other techniques used in the experiments due to the inner TV-regularization loop in A-step of OTVCA-CD and the SVD in V-step. Note that the CPU times for RF and SVM classifiers are greatly affected by the number of samples used.

TABLE V

CPU PROCESSING TIMES IN SECONDS CONSUMED BY DIFFERENT TECHNIQUES APPLIED ON TRENTO

	HSI	**EP**$_{\text{LiDAR}}$	**EP**$_{\text{HSI}}$	**EP**$_{\text{LiDAR+HSI}}$	OTVCA-fusion
SVM	11.99	15.97	50.30	78.44	390.18
RF	1.82	5.92	15.15	19.73	381.47

IV. CONCLUSION

In this paper, we proposed an innovative technique dedicated to the fusion of HSI and LiDAR. First, EPs were used to extract spatial and elevation information from HSI and LiDAR. The extracted EPs were modeled based on unknown fused features that live in a low-dimensional feature space. Then, OTVCA, which is a nonconvex optimization feature extraction technique, is utilized to estimate the unknown (low-dimensional) fused features.

We investigated the performance of the proposed method with two different data sets, captured over rural and urban areas. The classification accuracy has been obtained using RF and SVM classifiers for both rural and urban data sets. We demonstrated that the low-dimensional fused features obtained by the EPs and OTVCA improve the classification

accuracies compared with the integrated features for HSI and LiDAR using feature stacking. The experimental results confirm that the EPs can effectively extract spatial and elevation information from HSI and LiDAR, respectively. The results also show that OTVCA-fusion technique captures the redundancy of the features while improving the classification accuracies. The proposed approach significantly improved other approaches used for comparison (confirmed by McNemar's test) in terms of classification accuracy. In addition, the experiments showed that OTVCA-fusion provides classification maps having homogeneous regions while preserving the structures, which is due to the exploitation of the TV.

ACKNOWLEDGMENT

The authors would like to thank Prof. L. Bruzzone of the University of Trento for providing the Trento data set, the National Center for Airborne Laser Mapping for providing the Houston data set, and Prof. N. Yokoya for providing the shadow-removed HSI.

REFERENCES

[1] G. P. Asner *et al.*, "Invasive species detection in Hawaiian rainforests using airborne imaging spectroscopy and LiDAR," *Remote Sens. Environ.*, vol. 112, pp. 1942–1955, May 2008.

[2] G. A. Blackburn, "Remote sensing of forest pigments using airborne imaging spectrometer and LIDAR imagery," *Remote Sens. Environ.*, vol. 82, p. 311–321, Oct. 2002.

[3] M. Voss and R. Sugumaran, "Seasonal effect on tree species classification in an urban environment using hyperspectral data, LiDAR, and an object-oriented approach," *Sensors*, vol. 8, no. 5, pp. 3020–3036, 2008.

[4] R. M. Lucas, A. C. Lee, and P. J. Bunting, "Retrieving forest biomass through integration of CASI and LiDAR data," *Int. J. Remote Sens.*, vol. 29, no. 5, pp. 1553–1577, 2008.

[5] U. Heiden, W. Heldens, S. Roessner, K. Segl, T. Esch, and A. Mueller, "Urban structure type characterization using hyperspectral remote sensing and height information," *Landscape Urban Planning*, vol. 105, no. 4, pp. 361–375, Apr. 2012.

[6] R. K. Hall *et al.*, "Quantifying structural physical habitat attributes using LiDAR and hyperspectral imagery," *Environ. Monitor. Assessment*, vol. 159, pp. 63–83, Dec. 2009.

[7] B. Koetz, F. Morsdorf, S. van der Linden, T. Curt, and B. Allgöwer, "Multi-source land cover classification for forest fire management based on imaging spectrometry and LiDAR data," *Forest Ecol. Manage.*, vol. 256, pp. 263–271, Jul. 2008.

[8] M. D. Mura, S. Prasad, F. Pacifici, P. Gamba, J. Chanussot, and J. A. Benediktsson, "Challenges and opportunities of multimodality and data fusion in remote sensing," *Proc. IEEE*, vol. 103, no. 9, pp. 1585–1601, Sep. 2015.

[9] C. Debes *et al.*, "Hyperspectral and LiDAR data fusion: Outcome of the 2013 GRSS data fusion contest," *IEEE J. Sel. Topics Appl. Earth Observ. Remote Sens.*, vol. 7, no. 6, pp. 2405–2418, Jun. 2014.

[10] J. T. Mundt, D. R. Streutker, and N. F. Glenn, "Mapping sagebrush distribution using fusion of hyperspectral and LiDAR classifications," *Photogramm. Eng. Remote Sens.*, vol. 72, no. 1, pp. 47–54, Sep. 2006.

[11] R. Sugumaran and M. Voss, "Object-oriented classification of LiDAR-fused hyperspectral imagery for tree species identification in an urban environment," in *Proc. Urban Remote Sens. Joint Event*, Apr. 2007, pp. 1–6.

[12] P. Ghamisi, J. A. Benediktsson, and S. Phinn, "Land-cover classification using both hyperspectral and LiDAR data," *Int. J. Image Data Fusion*, vol. 6, no. 3, pp. 189–215, 2015.

[13] M. Dalponte, L. Bruzzone, and D. Gianelle, "Fusion of hyperspectral and LiDAR remote sensing data for classification of complex forest areas," *IEEE Trans. Geosci. Remote Sens.*, vol. 46, no. 5, pp. 1416–1427, May 2008.

[14] W. Liao, R. Bellens, A. Pižurica, S. Gautama, and W. Philips, "Generalized graph-based fusion of hyperspectral and LiDAR data using morphological features," *IEEE Geosci. Remote Sens. Lett.*, vol. 12, no. 3, pp. 552–556, Mar. 2015.

[15] G. Hughes, "On the mean accuracy of statistical pattern recognizers," *IEEE Trans. Inf. Theory*, vol. 14, no. 1, pp. 55–63, Jan. 1968.

[16] J. A. Benediktsson and P. Ghamisi, *Spectral-Spatial Classification of Hyperspectral Remote Sensing Images*. Boston, MA, USA: Artech House, 2015.

[17] P. Ghamisi, "Spectral and spatial classification of hyperspectral data," Ph.D. dissertation, Dept. Dep. Electr. Comput. Eng., Univ. Iceland, Reykjavik, Iceland, 2015.

[18] P. Ghamisi and J. A. Benediktsson, "Feature selection based on hybridization of genetic algorithm and particle swarm optimization," *IEEE Geosci. Remote Sens. Lett.*, vol. 12, no. 2, pp. 309–313, Feb. 2015.

[19] P. Ghamisi, M. S. Couceiro, and J. A. Benediktsson, "A novel feature selection approach based on FODPSO and SVM," *IEEE Trans. Geosci. Remote Sens.*, vol. 53, no. 5, pp. 2935–2947, May 2015.

[20] Y. Bazi and F. Melgani, "Toward an optimal SVM classification system for hyperspectral remote sensing images," *IEEE Trans. Geosci. Remote Sens.*, vol. 44, no. 11, pp. 3374–3385, Nov. 2006.

[21] P. Ghamisi, R. Souza, J. A. Beneiktsson, X. X. Zhu, L. Rittner, and R. A. Lotufo, "Extinction profiles for the classification of remote sensing data," *IEEE Trans. Geosci. Remote Sens.*, vol. 54, no. 10, pp. 5631–5645, Oct. 2016.

[22] L. I. Rudin, S. Osher, and E. Fatemi, "Nonlinear total variation based noise removal algorithms," *Phys. D, Nonlinear Phenomena*, vol. 60, nos. 1–4, pp. 259–268, 1992.

[23] F. Palsson, J. R. Sveinsson, and M. O. Ulfarsson, "A new pansharpening algorithm based on total variation," *IEEE Geosci. Remote Sens. Lett.*, vol. 11, no. 1, pp. 318–322, Jan. 2014.

[24] F. Palsson, J. R. Sveinsson, M. O. Ulfarsson, and J. A. Benediktsson, "SAR image denoising using total variation based regularization with sure-based optimization of the regularization parameter," in *Proc. IEEE Int. Geosci. Remote Sens. Symp. (IGARSS)*, Jul. 2012, pp. 2160–2163.

[25] Q. Yuan, L. Zhang, and H. Shen, "Hyperspectral image denoising employing a spectral–spatial adaptive total variation model," *IEEE Trans. Geosci. Remote Sens.*, vol. 50, no. 10, pp. 3660–3677, Oct. 2012.

[26] G. Martin, J. Bioucas-Dias, and A. Plaza, "Hyperspectral coded aperture (HYCA): A new technique for hyperspectral compressive sensing," in *Proc. IEEE Int. Geosci. Remote Sens. Symp. (IGARSS)*, Sep. 2012, pp. 1381–1384.

[27] M.-D. Iordache, J. Bioucas-Dias, and A. Plaza, "Total variation spatial regularization for sparse hyperspectral unmixing," *IEEE Trans. Geosci. Remote Sens.*, vol. 50, no. 11, pp. 4484–4502, Nov. 2012.

[28] J. Sigurdsson, M. O. Ulfarsson, J. R. Sveinsson, and J. A. Benediktsson, "Smooth spectral unmixing using total variation regularization and a first order roughness penalty," in *Proc. IEEE Int. Geosci. Remote Sens. Symp. (IGARSS)*, Jul. 2013, pp. 2160–2163.

[29] B. Rasti, J. R. Sveinsson, and M. O. Ulfarsson, "Total variation based hyperspectral feature extraction," in *Proc. IEEE Geosci. Remote Sens. Symp.*, Jul. 2014, pp. 4644–4647.

[30] B. Rasti, M. O. Ulfarsson, and J. R. Sveinsson, "Hyperspectral feature extraction using total variation component analysis," *IEEE Trans. Geosci. Remote Sens.*, vol. 54, no. 12, pp. 6976–6985, Dec. 2016.

[31] C. Vachier and F. Meyer, "Extinction value: A new measurement of persistence," in *Proc. IEEE Workshop Nonlinear Signal Image Process.*, vol. 1. Jun. 1995, pp. 254–257.

[32] P. Soille, *Morphological Image Analysis: Principles and Applications*, 2nd ed. Springer-Verlag, 2003.

[33] P. Ghamisi, R. Souza, J. A. Benediktsson, L. Rittner, R. Lotufo, and X. X. Zhu, "Hyperspectral data classification using extended extinction profiles," *IEEE Geosci. Remote Sens. Lett.*, vol. 13, no. 11, pp. 1641–1645, Nov. 2016.

[34] J. A. Palmason, J. A. Benediktsson, J. R. Sveinsson, and J. Chanussot, "Classification of hyperspectral data from urban areas using morphological preprocessing and independent component analysis," in *Proc. IEEE Int. Geosci. Remote Sens. Symp. (IGARSS)*, vol. 1. Jul. 2005, p. 4.

[35] W. Liao, R. Bellens, S. Gautama, and W. Philips, "Feature fusion of hyperspectral and LiDAR data for classification of remote sensing data from urban area," in *Proc. 5th Workshop EARSeL Special Interest Group Land Use Land Cover*, 2014, p. 34.

[36] B. Schölkopf, A. Smola, and K. R. Müller, "Nonlinear component analysis as a kernel eigenvalue problem," *Neural Comput.*, vol. 10, no. 5, pp. 1299–1319, 1998.

[37] G. M. Foody, "Thematic map comparison: Evaluating the statistical significance of differences in classification accuracy," *Photogramm. Eng. Remote Sens.*, vol. 70, no. 5, pp. 627–633, 2004.

Behnood Rasti (S'12–M'14) received the B.Sc. and M.Sc. degrees in electrical and electronics engineering from the University of Guilan, Rasht, Iran, in 2006 and 2009, respectively, and the Ph.D. degree in electrical and computer engineering from the Department of Electrical and Computer Engineering, University of Iceland, Reykjavík, Iceland, in 2014.

From 2015 to 2016, he was a Post-Doctoral Researcher with the University of Iceland. In 2016, he joined the Keilir Institute of Technology, Reykjavík, where he is currently an Instructor. His research interests include signal and image processing, hyperspectral image analysis, remote sensing data fusion, biomedical engineering, biomedical data analysis, control system, and robotics.

Pedram Ghamisi (S'12–M'15) received the B.Sc. degree in civil (survey) engineering from the Tehran South Campus of Azad University, Tehran, Iran, the M.Sc. degree (with first class Hons.) in remote sensing from the K. N. Toosi University of Technology, Tehran, in 2012, and the Ph.D. degree in electrical and computer engineering from the University of Iceland, Reykjavík, Iceland, in 2015.

From 2013 to 2014, he spent seven months at the School of Geography, Planning and Environmental Management, University of Queensland, Brisbane, QLD, Australia. He was a Post-Doctoral Research Fellow at the University of Iceland. In 2015, he won the prestigious Alexander von Humboldt Fellowship and has been a Post-Doctoral Research Fellow at the Technical University of Munich, Munich, Germany, and Heidelberg University, Heidelberg, Germany, since 2015. He has also been a Researcher at the German Aerospace Center and the Remote Sensing Technology Institute, Germany, since 2015. His research interests include remote sensing and image analysis, with a special focus on spectral and spatial techniques for hyperspectral image classification, multisensor data fusion, machine learning, and deep learning.

Dr. Ghamisi received the Best Researcher Award for M.Sc. students from the K. N. Toosi University of Technology, during 2010–2011. In 2013, he presented at the IEEE International Geoscience and Remote Sensing Symposium, Melbourne, VIC, Australia, and was awarded the IEEE Mikio Takagi Prize for winning the conference Student Paper Competition against almost 70 people. In 2016, he was selected as a talented international researcher by the Iran's National Elites Foundation.

Richard Gloaguen (M'05) received the Ph.D. degree in marine geosciences "Communitatis Europae" from the University of Western Brittany, Brest, France, in collaboration with the Royal Holloway University of London, London, U.K., and Göttingen University, Göttingen, Germany, in 2000.

He was a Post-Doctoral Research Associate at the Royal Holloway University of London from 2000 to 2003. He led the Remote Sensing Group at University Bergakademie Freiberg, Freiberg, Germany, from 2003 to 2013. Since 2013, he has been leading the division "Exploration Technology" at the Helmholtz-Institute Freiberg for Resource Technology, Freiberg. He is currently involved in UAV-based hyperspectral imaging, laser-induced fluorescence, and remote sensing-based tectonic geomorphology. His research interests include multisource multiscale remote sensing integration.